




Article

Fabrication of Ti₃Al-Based Intermetallic Alloy by Laser Powder Bed Fusion Using a Powder Mixture

Kuanhe Li ^{1,4}, Xianglong Wang ^{2,3,4}, Haishao Chen ^{5,*}, Xiaoxiao Huang ⁵, Guanglin Zhu ¹ and Ganfeng Tu ¹¹ School of Metallurgy, Northeastern University, Shenyang 110819, China² China Machinery Institute of Advanced Materials Co., Ltd., Zhengzhou 450001, China³ State Key Laboratory for Advanced Forming Technology and Equipment, China Academy of Machinery Science and Technology, Beijing 100083, China⁴ Mining and Materials Engineering, McGill University, 3610 University Street, Montreal, QC H3A 0C5, Canada⁵ School of Intelligent Manufacturing and Electronic Engineering, Wenzhou University of Technology, Wenzhou 325025, China

* Correspondence: 00195124@wzu.edu.cn

Abstract: Due to their light weight and outstanding mechanical properties at high temperatures, Ti₃Al-based intermetallic alloys have driven increasing interest from both academia and industry; however, when additive manufacturing (AM) is applied to them, the outcome is hardly satisfying. In this work, we report a crack-free Ti₃Al-based alloy fabrication by laser powder bed fusion (LPBF) using a mixture of a commercial Ti-48Al-2Cr-2Nb powder and a pure Ti powder. With the aid of a high cooling rate during LPBF, the as-built sample shows a ductile β phase with some partially-melted particles. After the heat treatment, partially-melted particles were dissolved, and the sample showed equiaxed α₂ precipitates in the β matrix. The hardness was 515 ± 38 HV in the as-built sample and 475 ± 37 HV in the heat-treated sample. This study shows a novel strategy to fabricate crack-free Ti₃Al-based alloy using LPBF from powder blends.

Keywords: laser powder bed fusion; additive manufacturing; Ti₃Al alloy; intermetallic alloy



Citation: Li, K.; Wang, X.; Chen, H.; Huang, X.; Zhu, G.; Tu, G. Fabrication of Ti₃Al-Based Intermetallic Alloy by Laser Powder Bed Fusion Using a Powder Mixture. *Materials* **2023**, *16*, 2699. <https://doi.org/10.3390/ma16072699>

Academic Editor: Irina Hussainova

Received: 17 February 2023

Revised: 11 March 2023

Accepted: 23 March 2023

Published: 28 March 2023



Copyright: © 2023 by the authors. Licensee MDPI, Basel, Switzerland. This article is an open access article distributed under the terms and conditions of the Creative Commons Attribution (CC BY) license (<https://creativecommons.org/licenses/by/4.0/>).

1. Introduction

Over the last 30 years, titanium aluminide intermetallic alloys, based on TiAl and Ti₃Al, have driven plenty of interest in high-temperature applications up to 650 °C, including turbine blades, engine components, etc. [1]. Compared to Ni superalloys and Ti alloys, titanium aluminide alloys possess various advantages at high temperatures, such as low density, outstanding strength, superior creep resistance, and good corrosion resistance, and are thus considered to be a promising candidate material for the next-generation superalloy [2,3].

As an advanced manufacturing technology, additive manufacturing (AM) has won growing attention, due to its advantages in complex lattice structure fabrication, near-net-shape production, and short lead time customization [4–6]. Hence, applying AM to titanium aluminide alloys has emerged as a research hotspot [7–11]. However, the sourcing of the powders is hindering the development of some material systems, including Ti₃Al alloys, due to the lack of commercialized powder and the high cost of customizing the pre-alloyed powders [12,13]. Therefore, LPBF with a powder blend would be an alternative method. Nevertheless, compositional homogeneity is the major concern of using powder blends for LPBF. The melting point difference of the powder ingredients apparently increases the possibility of inhomogeneity. Recently, some attempts were carried out based on powder blends, such as NiTi [14], Ti6Al4V [15,16], Fe-Cr-Ni [17], etc. However, some high-melt elements, e.g., Nb in the Ti2AlNb system [18], can significantly deteriorate the homogeneity of the material [19]. In this study, an assumption based on powder blends of commercially pure Ti (CP-Ti) and TiAl-4822 has been proposed. As nearly the only commercialized titanium

aluminide alloy, TiAl-4822 and its powders, with a nominal composition of Ti-48Al-2Cr-2Nb (at.%), can be easily sourced. The pre-alloyed powders naturally prevent the inhomogeneity of high-melt Nb. Additionally, the TiAl-4822 powders have a melting point of 1490 °C, similar to the CP-Ti powder (1668 °C). Therefore, the compositional homogeneity can be good and the difficulty of the following heat treatment (HT) can be reduced.

On the other hand, cracking is also a major barrier to achieving the fabrication of satisfying titanium aluminum alloys by AM [20–22]. The intrinsic brittleness of titanium aluminum alloys, accompanied by the rapid solidification and high residual stresses in most metal AM, leads to the cracking problem [23–25]. Ti₃Al-based alloys suffer from low ductility at ambient temperature, primarily due to the high-volume fraction of the hcp α_2 phase (D0₁₉). This ordered hexagonal structure provides limited slip systems during deformation, which are not enough to sufficiently accommodate dislocation slip, thus resulting in the inherent brittleness of Ti₃Al-based alloys at room temperature [26]. To deal with this drawback, the introduction of the ductile β phase is considered to be a possible solution because it features a symmetric cubic structure with sufficient slip systems. The presence of the β phase at room temperature can be achieved in Ti₃Al alloys, mainly by adding β -solidifying elements such as Mo, Nb, V, and Cr [1,27]. Therefore, based on the β/α_2 duplex structure, several alloy compositions such as super α_2 alloy (Ti-25Al-10Nb-3V-1Mo, at.%) [28,29], Ti-24Al-11Nb (at.%) [30], etc., have been investigated and developed. In these studies, however, high volume fractions of β phase have not been obtained, whereas the high amount of Nb addition also significantly increases the density and production cost of the alloys. Recently, some research has reported that unique phase constitutions may be formed due to the rapid solidification conditions of metal AM processes, which may introduce out-of-equilibrium phases (e.g., β phase), providing an alternative way of controlling phase constituents other than the addition of alloying elements. For example, the disordered β phase was achieved using laser powder bed fusion (LPBF) to increase the ductility in a Fe-Co intermetallic system [31]. Durejko et al. [32] also showed the modulation of D0₃/B2 phase proportion in an Fe₃Al system by controlling AM parameters. Our previous study suggested that, with the aid of a high cooling rate in LPBF, TiAl-4822 showed a high fraction of β phase [33]. The Ti₃Al alloy undergoes a wider β phase field during cooling, and thus a high fraction of disordered β can be expected, which secures the components from the initial cold cracking.

In this study, the Ti₃Al-based alloy was processed by LPBF from a CP-Ti and TiAl-4822 powder blend. The crack-free thin strut sample has been accomplished as fundamental research for the AM-aided complexed lattice structure. The phases, microstructure, and texture evolution were characterized by X-ray diffraction (XRD), scanning electron microscope (SEM), electron dispersive spectrometer (EDS), and electron backscattered diffraction (EBSD). After the HT, the partially-melted particles were fully dissolved, and an α_2/β duplex structure was achieved. The microhardness was also investigated to show the mechanical property. This study shows a novel strategy to process Ti₃Al-based alloy using LPBF from powder blends.

2. Materials and Methods

The powder feedstocks were Ti-48Al-2Cr-2Nb (TiAl-4822) powder and pure Ti powder. The commercial TiAl-4822 powder was sourced from AP&C Company, with a nominal composition of Ti-48% Al-2% Nb-2%Cr (at.%). Pure Cp-Ti powder was also sourced from AP&C Company. The powder blend consisted of 56 g CP-Ti powders for every 100 g TiAl-4822 powder. The powders were mixed and homogenized in a tumbler mixer for 4 h. A rolling mill drives the tumbler container to rotate, with the powder blend in, and in this way the powder blend was mixed. The powder size distribution was characterized by an LA-920 Horiba laser particle size analyzer, and the morphology and chemical composition were analyzed using a Hitachi SU3500 SEM with an EDS. For phase characterization, a Bruker D8 Discovery X-ray diffractometer with a Cu radiation source was used under a 2 θ range of 15–100 degrees.

Strut samples with a nominal diameter of 1 mm were fabricated, using a customized LPBF system equipped with a pulsed Ytterbium fiber laser having a maximum power output of 25 W in a pure Ar atmosphere. The experimental parameters were as follows: The laser beam focus diameter is 110 μm , the laser scanning speed is 150 mm/min, the laser frequency is 25 pulses per second, the exposure time of each pulse is 0.8 ms, the hatch spacing is 100 μm , and the layer thickness is 50 μm . The substrates used in the experiments were commercial Ti-6Al-4V plates. HT at 1185 $^{\circ}\text{C}$ for 4 h was applied to the as-built samples.

Before metallurgical characterization, the as-built and HT samples were sectioned along the transverse direction, followed by sequential grinding steps up to 800 grit using SiC grinding papers. The polishing steps were done using 9 μm , 3 μm , and 1 μm diamond suspensions. Finally, the samples were polished with 0.05 μm colloidal silica suspension in a Vibromet 2 machine for 30 h.

To identify the phase of the as-built and HT samples, the Cu source Bruker D8 XRD was used, where the scans were carried out within a 2θ range of 15 to 100 degrees with a step size of 0.005 degrees. To reveal the microstructure, a Keyence VHX-S550E optical microscope and the Hitachi SU3500 SEM equipped with an EDS detector were utilized. For the crystallographic texture analysis, an EBSD system mounted on the Hitachi SU3500 SEM was utilized. The acquisition was conducted at an accelerating voltage of 15 keV and a step size of 2.2 μm and 0.5 μm . After the acquisition, the raw data were processed with the HKL Channel 5 software.

To investigate the mechanical properties, Vickers microhardness measurement was conducted with a CM-100AT Clark Microhardness Indenter to obtain hardness profiles of the samples. The tests were performed at a load of 300 gf.

3. Results and Discussion

3.1. Powder Mixture Characterization

The powder morphologies of the powder mixture, TiAl-4822, and CP-Ti were shown in Figure 1a, indicating similar spherical shapes and smooth surfaces. The selected TiAl-4822 and the CP-Ti also showed close powder size distributions, as shown in Figure 1b. The D_{10} , D_{50} , and D_{90} of TiAl-4822, CP-Ti, and the mixture are shown in Table 1.

Table 1. D_{10} , D_{50} , and D_{90} of TiAl-4822, CP-Ti, and the powder feedstock mixture.

	D_{10} (μm)	D_{50} (μm)	D_{90} (μm)
TiAl-4822	25.36	33.9	45.27
CP-Ti	27.44	40.06	56.40
Mixture	25.36	36.05	53.47

Figure 2a–e show the BSE image on the powder's cross-section and the corresponding EDS maps of Al, Ti, Cr, and Nb, respectively. Figure 2a highlights a large fraction of spherical particles with low porosity. It is worth noting that Figure 2c contains some darker green regions, indicating a relatively lower Ti content, which corresponds well with the contrasts in the EDS maps of Al, Cr, and Nb in Figure 2b,d,e. Therefore, these regions represent the TiAl-4822 powders. On the other hand, the brighter green regions in Figure 2c were identified as CP-Ti powder since the same regions did not show Al, Cr, and Nb signals. The EDS maps indicated that a homogeneous mixture was achieved and was qualified to be the feedstock for LPBF.

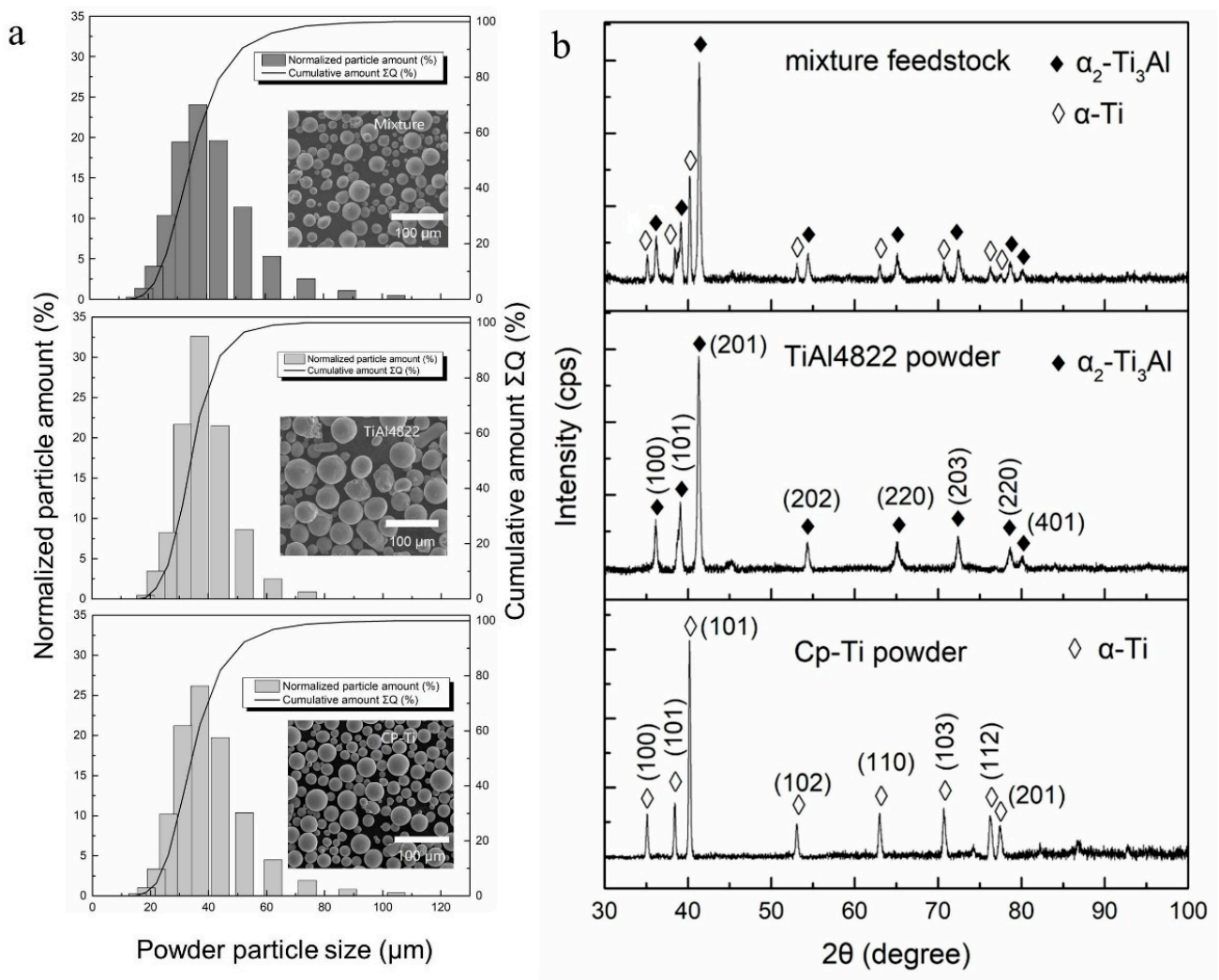


Figure 1. (a) Histogram of powder size distribution and the corresponding powder morphologies of the powder mixture, TiAl-4822, and Cp-Ti; (b) XRD patterns of the mixture, TiAl-4822, and Cp-Ti powders.

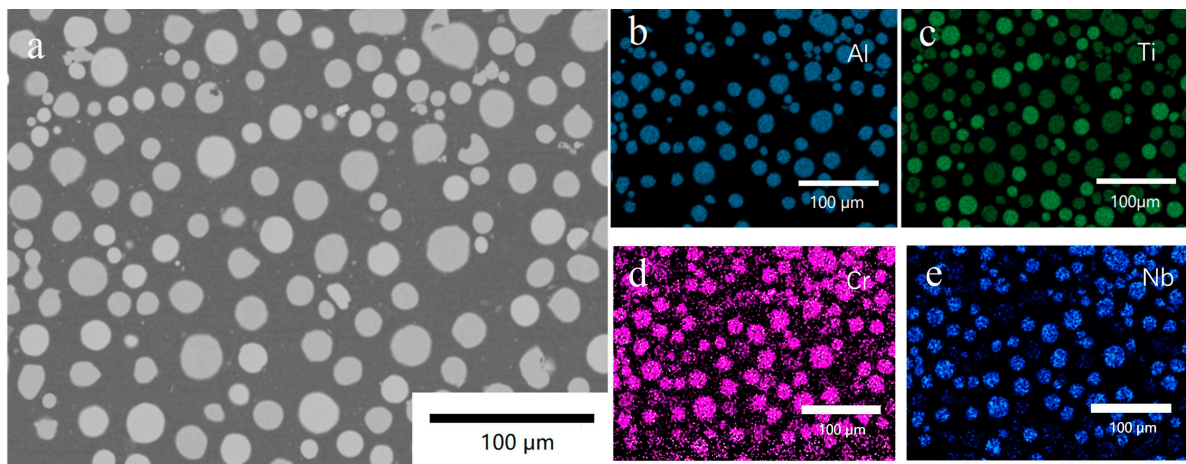


Figure 2. (a) BSE image of the cross-section of powder mixture from TiAl4822 and pure Ti powders, and EDS map of (b) Al, (c) Ti, (d) Cr, (e) Nb.

3.2. Characterization of the As-Built Sample

The XRD patterns of the as-built sample and powder mixture feedstock are shown in Figure 3, with the thin strut sample fabricated by LPBF inserted. Compared with the XRD pattern of the powder mixture of CP-Ti and TiAl-4822, the as-built sample consisted of nearly a single β phase. No large fraction of the α phase from CP-Ti was detected. This may contribute to the small amount of unmelted CP-Ti powder, whose major peak is at 40.161° (JCPDS: 65-9622) and coincides with the (100) β peak. The presence of these particles will be discussed using BSE and EBSD characterization later. A small amount of α_2 phase can be confirmed by the diffraction peak at 41.035° (JCPDS: 65-7534). This small amount of α_2 phase can be considered mainly as the partially-melted TiAl-4822 in the heat-affected-zone. In the β -solidifying Ti_3Al alloys, the transformation from disordered β to its ordered counterpart β_0 (B2) has been widely reported [34,35]. This ordered phase is regarded as detrimental to room-temperature ductility [35]. The switch of lattice parameters from 0.3206 nm to 0.3186 nm is a criterion to identify the disordered β phase and ordered β_0 phase. The small number of alloying elements provides limited influence on the lattice parameters, typically at the order of 0.0001 nm. Based on the XRD pattern, the lattice parameter was calculated to be 0.3208 nm, matching with the β phase lattice parameter reported by Holec et al. [34], implying the presence of a high fraction of disordered β phase in the as-built sample. In addition, with the increase of Nb, the ordering temperature of β/B_2 , increases [36], which suppresses the ordering transition and increases the possibility of β phase. Essentially, the high cooling rate (at the level of 10^5 – 10^7 K/s [23,37]) generated by the pulsed laser facilitates the formation of the β phase. The disordered β is intrinsically ductile and could accommodate the potential cracking propagation, securing the components from the initial cracking [33]. It should be also noted that the thin strut structure has relatively low residual stress in the LPBF fabrication. To scale up the strut component, more investigation is also required to control the content and distribution of the β phase and the partially-melted particles to resist the negative effect of scaling up.

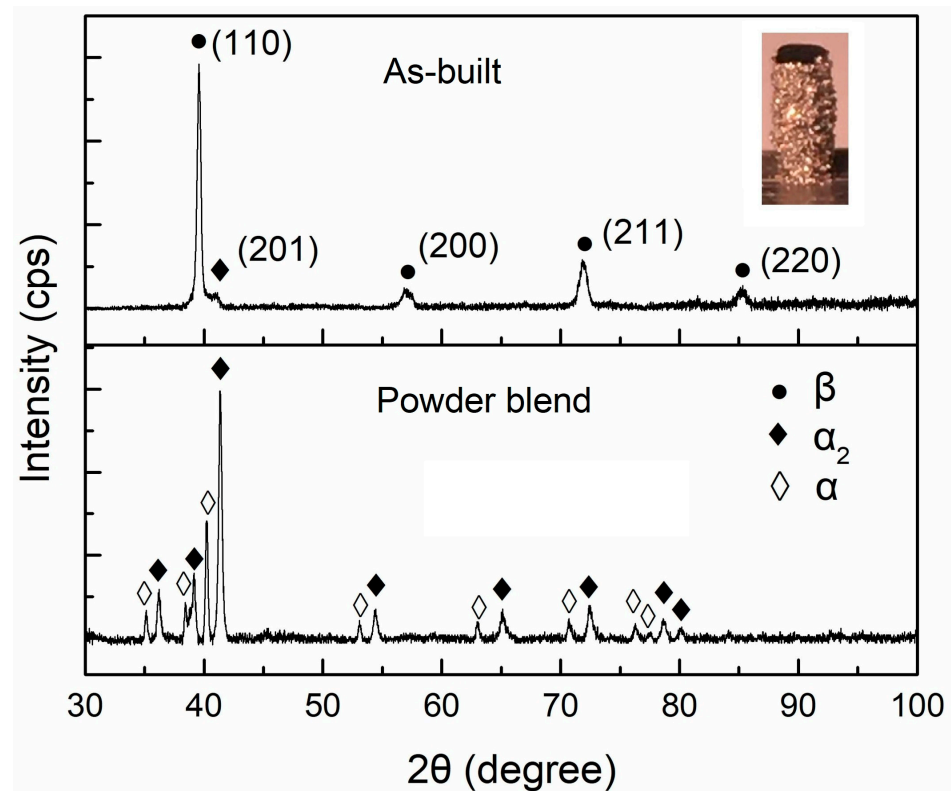


Figure 3. XRD patterns of the as-built sample and powder mixture feedstock, with an inserted picture showing the appearance of the rod sample prepared by LPBF.

BSE image of the as-built sample was shown in Figure 4a without showing any cracks. This phenomenon gives an optimistic expectation in the Ti_3Al complex lattice structure manufacturing in the future. One of the concerns of the powder mixture LPBF is the sufficiency of the melting and the chemical homogeneity. The EDS maps in Figure 4b–e show that the as-built sample had a comparably good homogeneity, despite some partially-melted particles. Some of the particles have a thin plate-like shape, and others showed a near-spherical shape. The relative density of the partially-melted particles is $\sim 8\%$ in total, and the unmelted particles were more frequently observed near the edge of the strut sample. A partially-melted particle was shown using higher magnification in Figure 4a, and its corresponding EDS map is shown in Figure 4b–e.

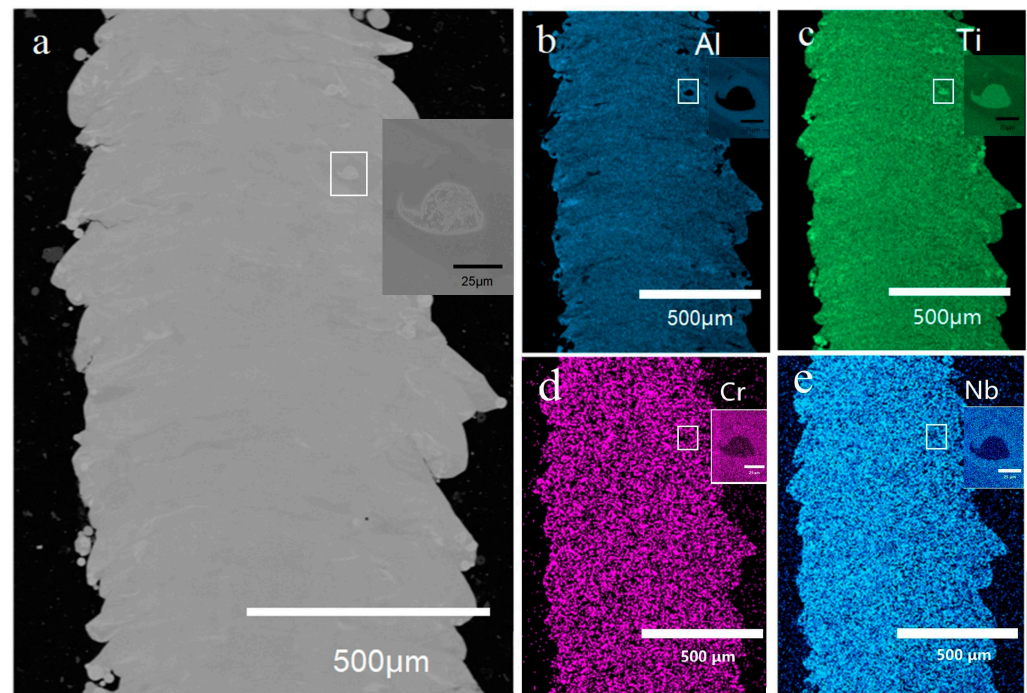


Figure 4. (a) BSE image of the as-built sample cross-section by LPBF, (b) EDS map of Al, (c) map of Ti, (d) map of Cr, (e) map of Nb.

A schematic in Figure 5 illustrates the presence of partially-melted Ti particles in the as-built sample. CP-Ti has a higher melting point ($1668\text{ }^{\circ}\text{C}$) than both TiAl-4822 ($\sim 1490\text{ }^{\circ}\text{C}$) [38] and the idealistic Ti_3Al mixture ($\sim 1610\text{ }^{\circ}\text{C}$). In the center of the melt pool, the temperature is high enough, and thus it is sufficient to obtain a well-stirred mixture. However, the heat-affected zone is below the liquidus of the Ti_3Al mixture at $\sim 1610\text{ }^{\circ}\text{C}$ and above the solidus at $\sim 1640\text{ }^{\circ}\text{C}$. When the Ti particle happens to be on the edge of the heat-affected zones, the melting can be insufficient, and the particles were sintered. Some of the partially-melted particles are located near the surface, which can be remelted by the overlapping of the next melt pool (shown in the dashed line). In the peripheral region of the sample, it was not as possible to sufficiently remelt it. Therefore, the number of partially-melted particles increased. If the partially-melted particles were at the bottom of the heat-affected zone, they could not be remelted by the overlapping. In the same scenario, TiAl-4822 particles can also be sintered. As a result, partially-melted particles were observed.

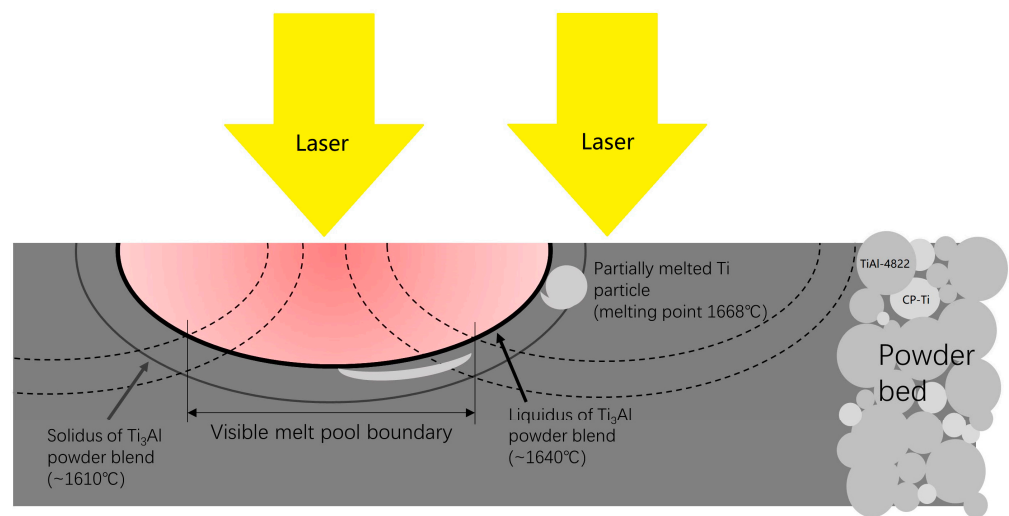


Figure 5. Schematic showing the formation of the partially-melted particles.

The BSE image in Figure 6a shows a typical central region of the as-built sample, with the melt pool represented by the dashed lines. Based on the EDS maps shown in Figure 6 b–e, Al segregation was observed associated with the melt pool shapes. The lack-of-Al regions were found along the melt pool boundaries. This phenomenon can be explained by the continuous growth model (CGM) developed by Aziz et al. [39]. In a non-equilibrium solidification, with the increase of the solidification front velocity, the solute partitioning effect is largely different from the equilibrium. At the bottom of a melt pool, the solidification front velocity is relatively lower, and Al segregates generally following the equilibrium phase diagram. With the increase of the solidification velocity, the segregation becomes insufficient, and Al content piles up to the melts. Therefore, the central region of a melt pool has a relatively higher Al content, and the Al-lack region corresponds to the bottom of the melt pools.

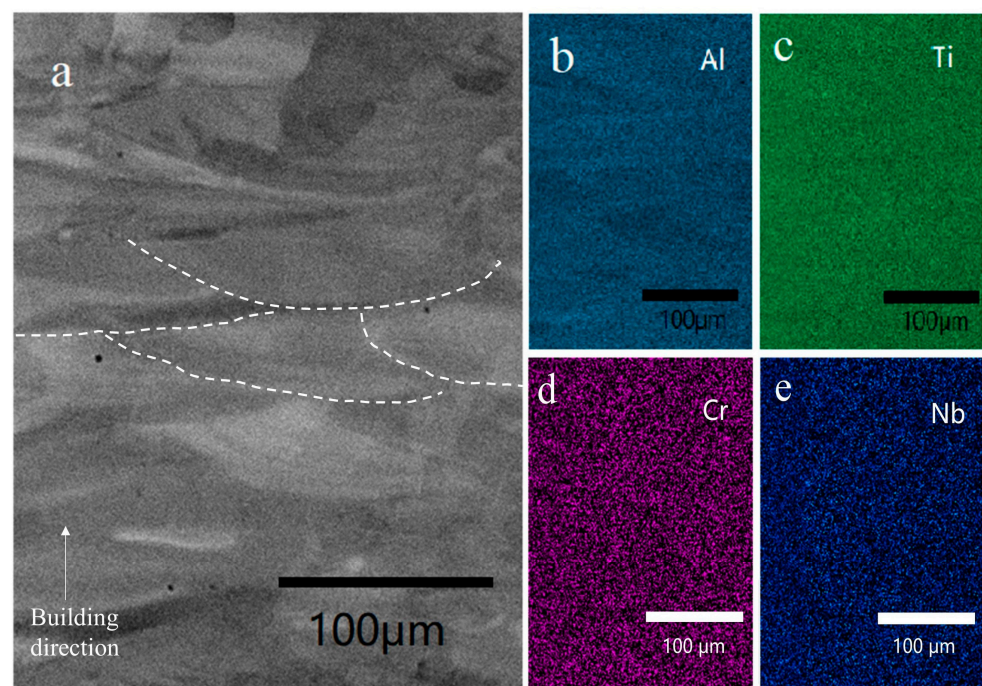


Figure 6. (a) BSE image of the central region of the as-built sample, and EDS maps of (b) Al, (c) Ti, (d) Cr, and (e) Nb.

To further understand the solidification process and the microstructure, EBSD was applied, and the results are shown in Figure 7. Figure 7a is the phase map, indicating that the as-built sample has a large fraction of β phase and some partially-melted particles dispersed in the β matrix. The fraction of β phase was measured to be 94.7%. With the aid of the ductile β phase, the intrinsically brittle Ti_3Al could be fabricated without cracks, regardless of the negative effect of high residual stress. It should be noticed that EBSD can not differentiate α and α_2 phases in this condition, and thus the partially-melted particles could be either of them. Figure 7b is the inverse pole figure. The shape of the β grains was irregular and asymmetrical, and some large grains grow through multiple layers, showing a sign of epitaxial growth. The epitaxial growth during LPBF typically follows the maximum heat flow direction based on the local curvature of the melt pools [23]. In this study, the partially-melted particles can affect the curvature of a melt pool and the grain growth direction.

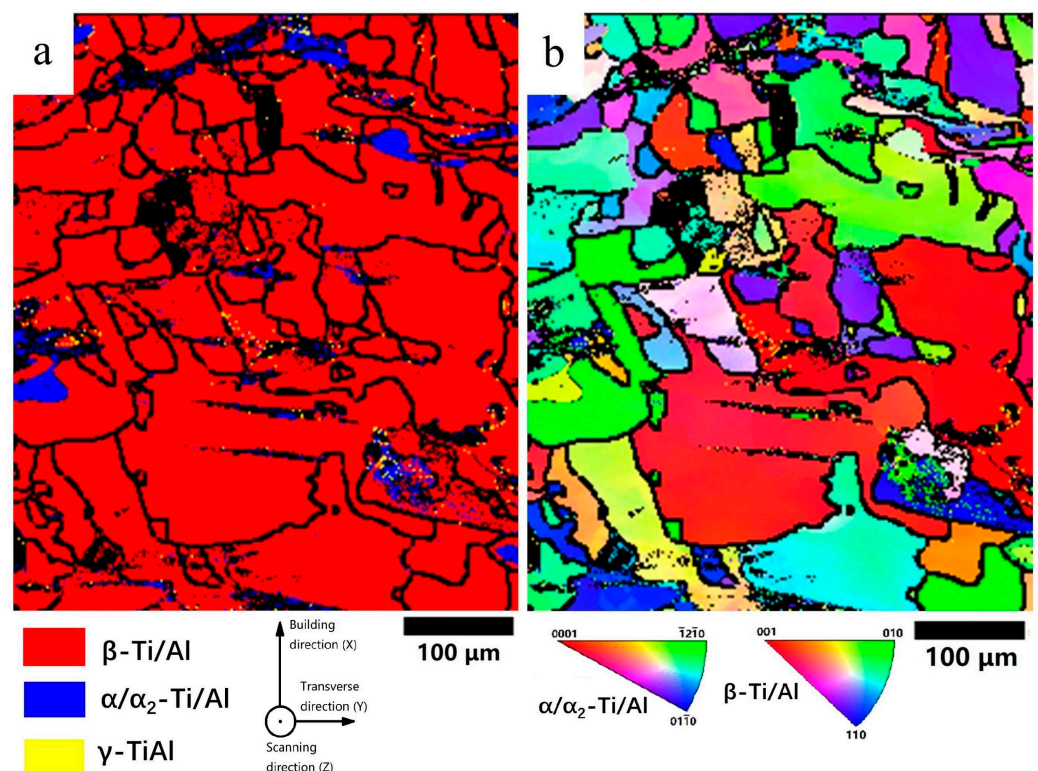


Figure 7. (a) EBSD colored phase map and (b) inverse pole figure colored map of the as-built sample.

3.3. Characterization of the Heat-Treated Sample

To achieve a satisfying homogeneity, an HT at 1200 °C (β single phase region) for 4 h, followed by air cooling, was applied. With the aid of XRD, phase evolution was revealed, as shown in Figure 8. Compared with the as-built sample, the HT sample contained a higher fraction of α_2 phase, which was very low in the as-built sample. The β phase fraction decreases in the HT sample, and the lattice parameter of the β phase was 0.32062 nm, which indicates that it remains a disordered β phase. This phenomenon is different from some previous studies, where the ordering transition from β to B2 takes place during air cooling [40–42]. This phenomenon can be attributed to the low Nb fraction at ~2 wt.%. In the pseudo-binary phase diagram of Ti_3Al -Nb by Strychor [43], the low Nb region maintains the β phase instead of the B2 phase. The study on Ti-25.2 at.% Al by differential thermal analysis and differential scanning calorimetry also support this understanding [44]. The β phase is considered to be beneficial to ductility and deformability, which is crucial to controlling the cracking susceptibility during AM. It can be expected that the Ti_3Al alloy with a low Nb content can be a promising candidate in the AM society.

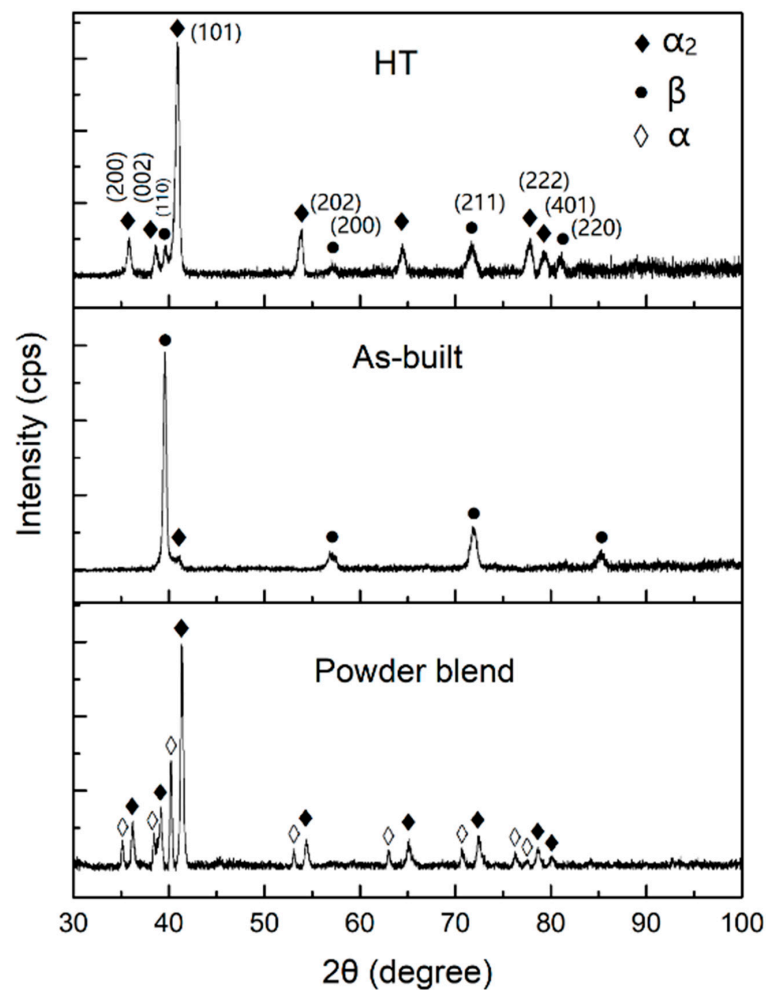


Figure 8. XRD patterns of the as-built sample and powder mixture feedstock.

As shown in Figure 9a, the BSE image of the HT sample shows no partially melted particles. The fine recrystallized α_2 -Ti₃Al equiaxed grains were observed in a darker contrast dispersed in the β phase matrix. Some of the equiaxed α_2 grains aligned in a row, along the building direction. The equiaxed α_2 structure has been reported [45]. The EDS maps of Al, Ti, Cr, and Nb are shown in Figure 9b–e. The Al and Ti distributions show a good homogeneity; however, as β -stabilizing elements, both Cr and Nb favor β phase domains.

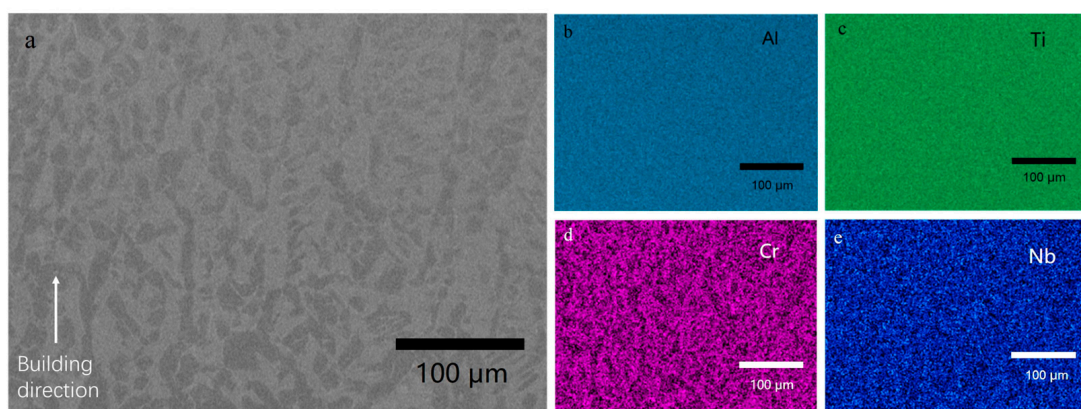


Figure 9. (a) BSE image of the HT sample, and EDS map of (b) Al, (c) Ti, (d) Cr, (e) Nb.

Figure 10a shows a BSE image at a higher magnification. In the equiaxed α_2 grains, some lamellar structures can be observed. In Figure 10d, the β phase region has a higher Cr content, and the α_2 region contains limited Cr. In Figure 10e, Nb also shows a similar trend; however, the segregation is not as obvious as Cr, indicating that Nb exists not only in the β phase but also in the α_2 phase with a small amount.

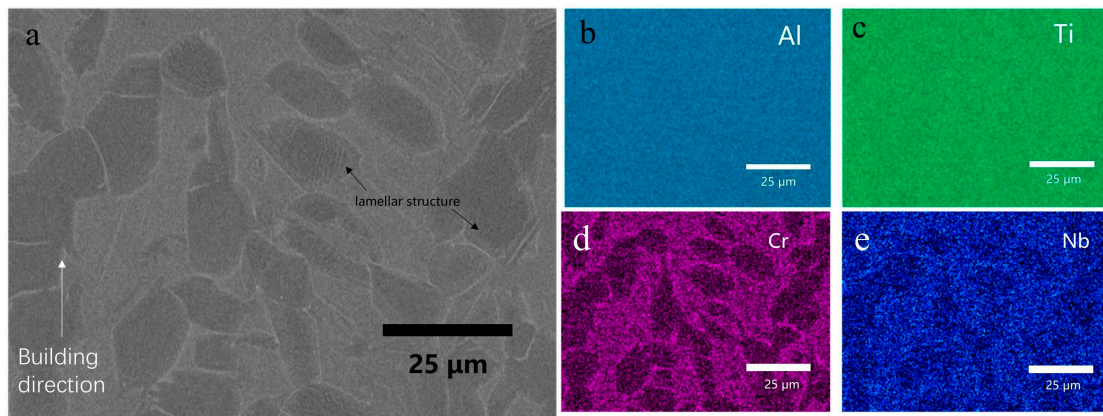


Figure 10. (a) BSE image of the HT sample at a higher magnification, EDS map of (b) Al, (c) Ti, (d) Cr, and (e) Nb.

To understand the recrystallization behavior of the α_2 grains, EBSD was carried out, as shown in Figure 11. Figure 11a shows the phase map, confirming the equiaxed fine grains consist of α_2 phase and the matrix is β phase. The average grain size of the α_2 phase was measured to be $15 \pm 4.7 \mu\text{m}$, and the average size of β grains was $19.4 \pm 9.5 \mu\text{m}$. α_2 phase contained a 60.3% area fraction of the indexed region, and the β phase contained 39.7%.

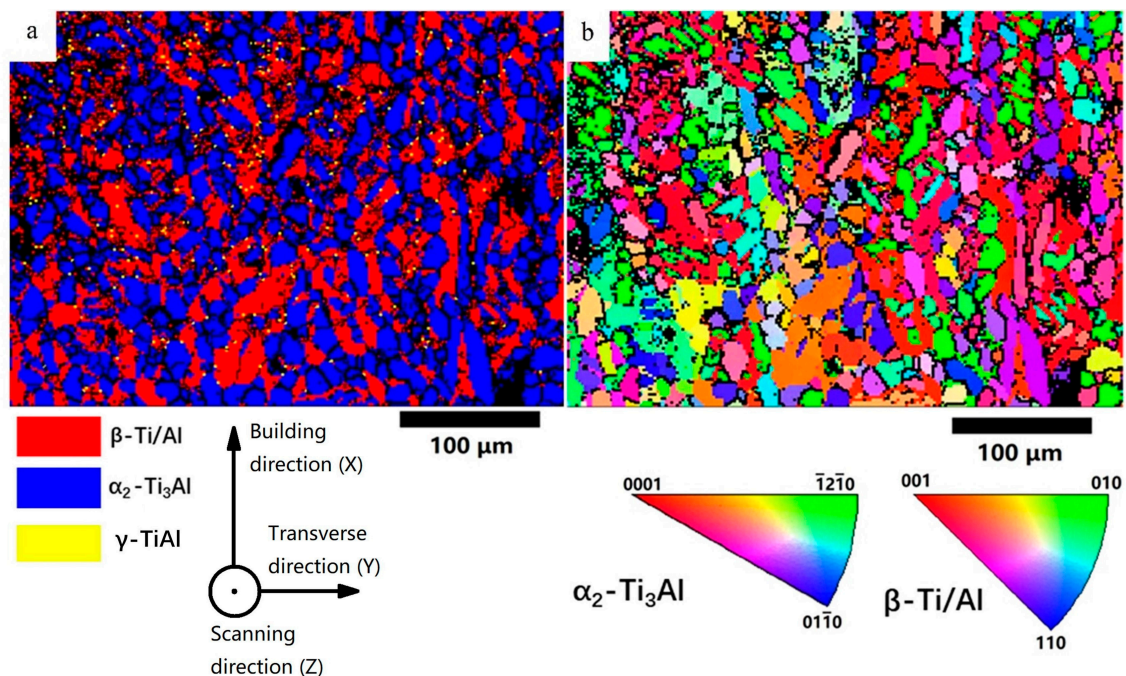


Figure 11. (a) EBSD phase distribution image of the HT sample, (b) inverse pole figure of the HT sample.

Figure 12a,b show the pole figures of the β and α_2 phases in the HT Ti_3Al sample, respectively. In contrast, Figure 12c illustrated the pole figure of the β phase in the as-built Ti_3Al sample. In the as-built sample, the β phase does not show a strong texture (MUD = 5.88), however after the HT, a strong $\langle 100 \rangle$ fiber texture (MUD = 22.43) with a

small mismatch angle of $\sim 10^\circ$ from the building direction was found. This crystallographic texture is widely reported in the thin structure LPBF of the materials with a cubic crystal structure [46,47]. The fact that the fiber texture was not strong in the as-built sample can be partially attributed to the presence of the partially-melted particles, which hinders the epitaxial growth of the β grains. During the HT, the partially-melt particles dissolve in the matrix at the temperature above the β - α transit ($\sim 1170^\circ\text{C}$, according to the equilibrium phase diagram [48]). Comparing the pole figure of HT $\alpha_2\{0001\}$ with HT $\beta\{110\}$, some crystallographic orientations align (labeled with dashed circles), which follows the Burgers orientation relationship (BOR), namely $(0001)_\alpha // (110)_\beta$, $\langle 11\bar{2}0 \rangle_\alpha // \langle 11\bar{1} \rangle_\beta$ [49]. The pole figures of HT $\alpha_2 \langle 11\bar{2}0 \rangle$ and HT $\beta \langle 11\bar{1} \rangle$ in Figure 12d also revealed this relationship. As far as the authors' knowledge, this is the first time that BOR was observed between α_2 and β phase in a Ti_3Al alloy. α_2 phase nucleates at the β grain boundaries, obeying BOR, and precipitates preferentially along with its $\{1000\}$ pole, resulting in this observation by the pole figures.

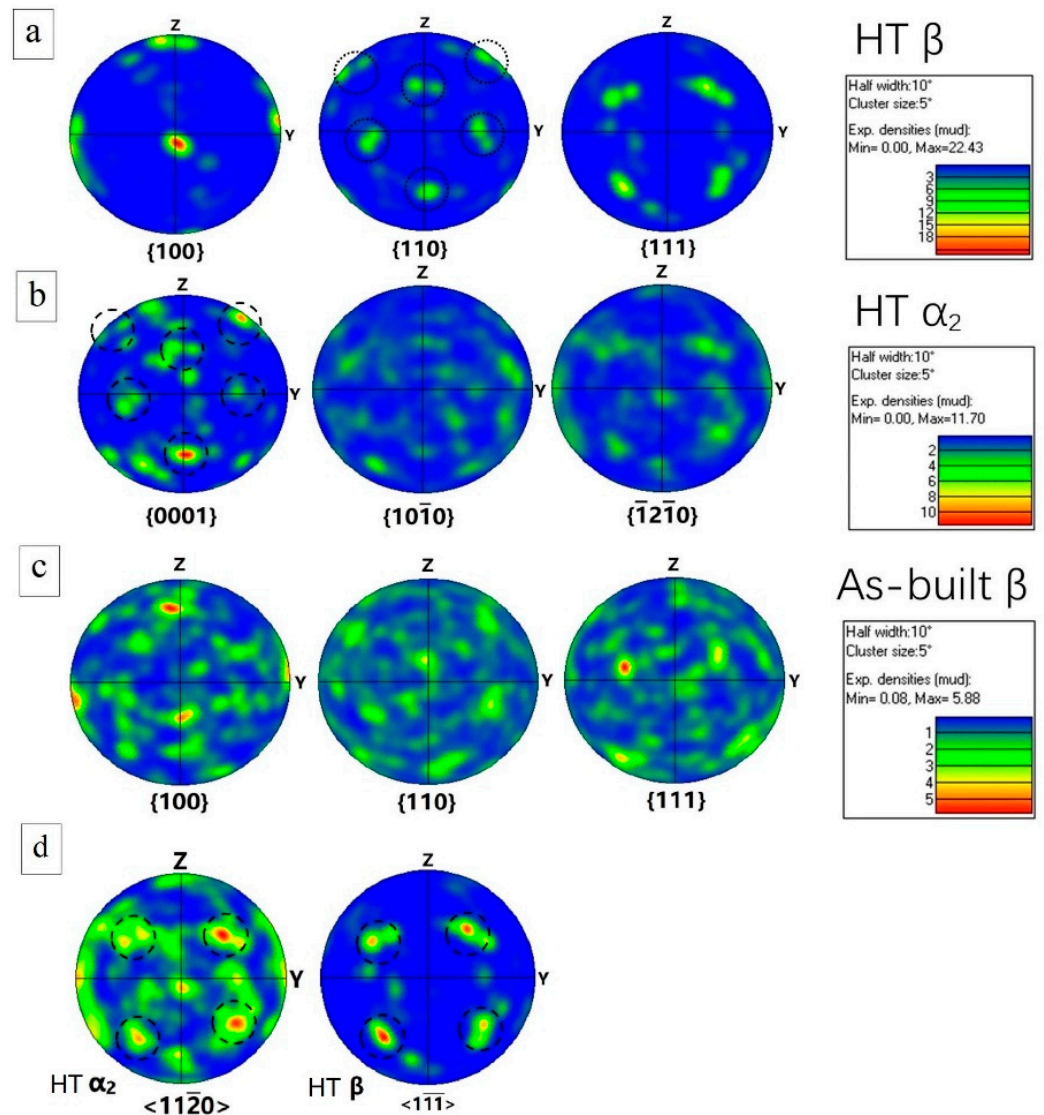


Figure 12. The pole figure of (a) HT β phase sample, (b) HT α_2 , (c) as-built β , (d) HT $\alpha_2 \langle 11\bar{2}0 \rangle$ and HT $\beta \langle 11\bar{1} \rangle$, showing the texture evolution after the heat treatment.

Figure 13a,b show the phase map and IPF of a region in the HT sample with a higher magnification, and Figure 13c shows the pole figures of HT α_2 {0001} and HT β {110}. It can be observed that the {0001} planes of α_2 1, α_2 2, and α_2 6 are parallel to the {110} planes of β 1, {0001} planes of α_2 3, α_2 4, and α_2 7 are parallel to the {110} planes of β 2, and the {0001} planes of α_2 5 and α_2 8 are parallel to the {110} planes of β 3. Respecting the Burgers orientation relationship, 12 hexagonal variants can be generated based on the parent β phase. Each α_2 precipitation selected a preferential orientation on the grain boundaries of β 1, β 2, and β 3 following BOR, and maintain the common {0001} pole in each α_2 grain. This transformation mode has been repeatedly reported in the near- α titanium alloys [50,51], as a valuable understanding in controlling the crystallographic orientation and microstructure via HT [52,53]. Another preferential orientation selection of the α phase in near- α titanium alloys has also been reported, which is related to the pre-existed α [50]. Due to the presence of partially-melted CP-Ti particles (consisting of α phase) in the as-built sample, this mode should also be considered possible; however, this mode is hardly proved in the present study, which requires more detailed investigation in the future.

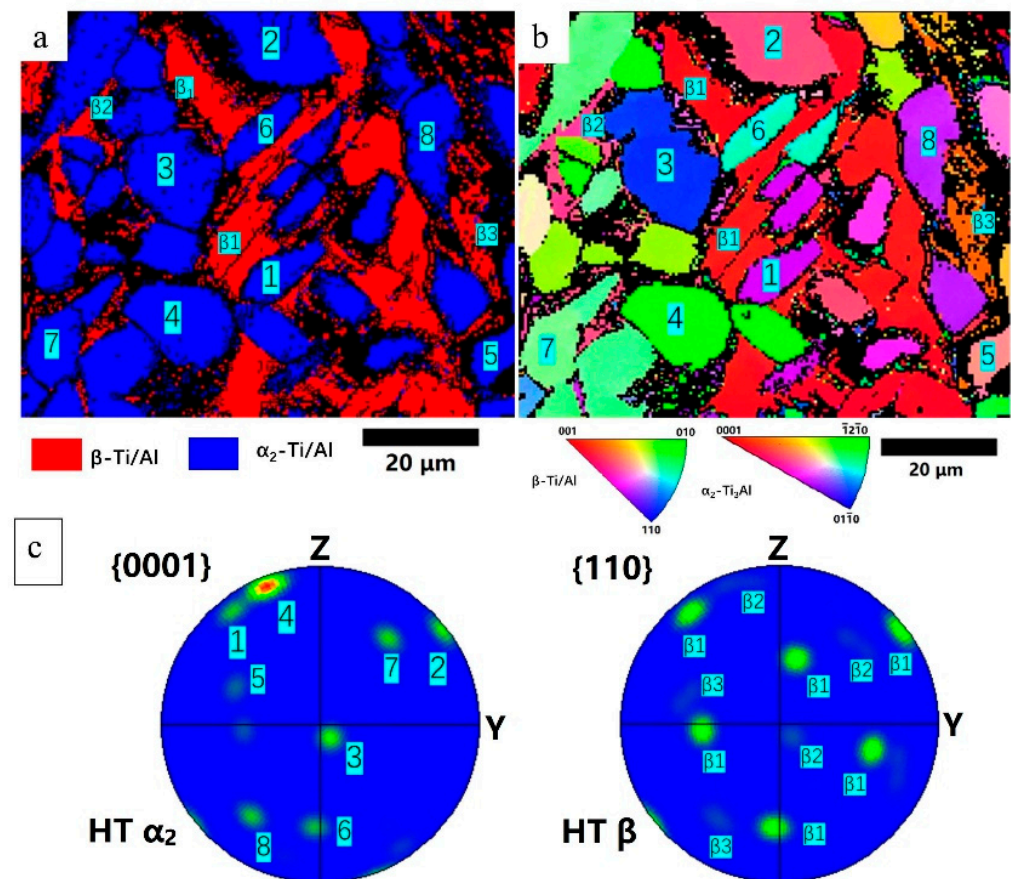


Figure 13. The orientation relationship in the HT sample: (a) phase distribution, (b) IPF, (c) pole figure of HT α_2 {0001} and HT β {110}.

3.4. Microhardness

Microhardness was tested for the as-built and HT samples to exhibit the mechanical property, as illustrated in Figure 14. The microhardness values of different heights in the as-built sample are relatively similar, and the highest values appeared at 2 mm from the substrate. After the HT, the microhardness values of different heights all decreased. The as-built sample and HT sample showed the average microhardness of 515 ± 38 HV and 475 ± 37 HV, respectively, as presented in Table 2. This decrease in the HT sample can be contributed to both the high dislocation density in the as-built sample and the high heat

treatment temperature used in this study. Typically, the LPBF process generates a huge number of dislocations in the as-built sample, which could lead to very high strength and hardness, along with low ductility [54,55]. After the heat treatment, the dislocation density decreases, and thus the ability to accommodate the deformation increases. As a result, the ductility increases, with a reduction in strength and hardness [55]. On the other hand, the HT in this study mainly aimed to dissolve the partially-melt particles in the as-built sample. Therefore, the HT temperature was relatively high, which is above the β transus. Typically, this HT condition leads to an increase in ductility but a decrease in strength and hardness [56]. Microhardness results from the previous studies regarding titanium aluminide intermetallics, also shown in Table 2, which showed inferior microhardness values compared with those of the as-built and HT samples in the present research. The values vary from 332 ± 18 HV to 510 HV, with different processing conditions, where the composition, processing condition, corresponding phase constituent, and microstructure affect the values. This comparison shows a promising research value of the method in this study in terms of microhardness.

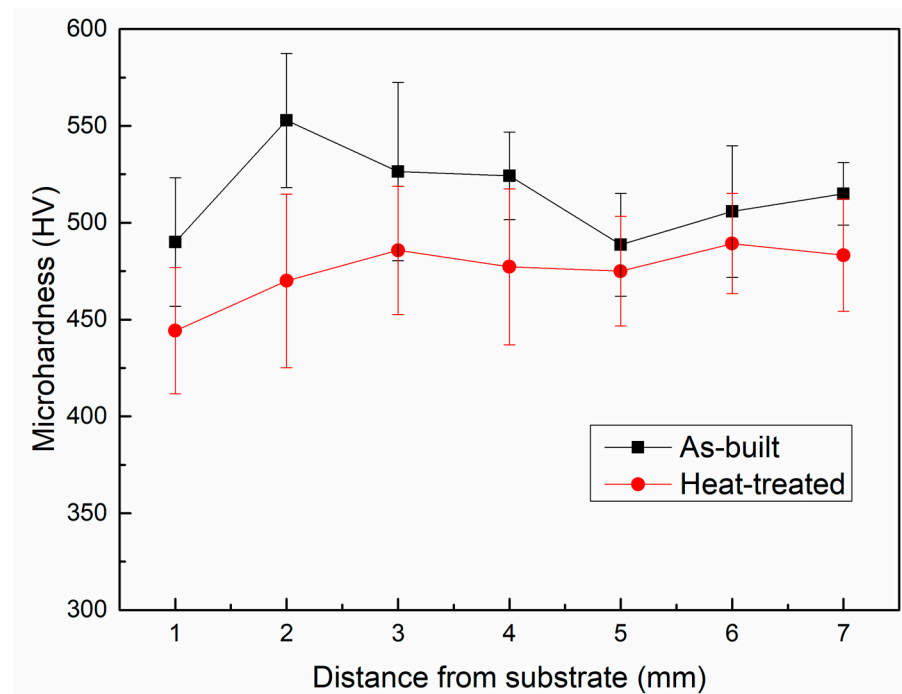


Figure 14. Microhardness of the as-built sample and heat-treated sample.

Table 2. Microhardness of some Ti_3Al alloys.

Composition	Method	Phase	Hardness (HV)	Reference
Ti-23Al-17Nb (at.%)	Linear friction welding	β , α_2 , O ¹	448	Li et al. [57]
Ti-24Al-11Nb (at.%)	Hot roll + quenching	β /B2, α_2	443	Suwas et al. [30]
Ti-22Al-12Nb (at.%)	Arc melting + hot vacuum pressing	B2, α_2	510 (Arc melting) 392 (hot pressing)	Kumar et al. [42]
Ti-22Al-25Nb (at.%)	EB ² welding	α_2 , O, B2	335 (as-weld), 420 (HT)	Chen et al. [58]
Ti-10Al-27Nb (wt.%)	EB welding	B2	342	Feng et al. [20]
Ti-22Al-25Nb (at.%)	LPBF ³ + HIP ⁴	α_2 , O, B2	332 ± 18	Polozov et al. [19]
Ti-22Al-25Nb (at.%)	LPBF + HT	α_2 , O, B2	338.6 ± 7.4 (as-built) 358.1 ± 5.8 (HT)	Grigoriev et al. [18]
Ti-33Al-1.4Cr-1.4Nb (at.%)	LPBF	β (as-built), $\alpha_2 + \beta$ (HT)	515 ± 38 (as-built), 475 ± 37 (HT)	This study

¹ O represents the orthorhombic phase [1]; ² EB represents electron beam; ³ LPBF represents laser powder bed fusion; ⁴ HIP represents hot isostatic pressing.

4. Conclusions

In this study, a crack-free fabrication of Ti₃Al-based alloy was performed by LPBF with a powder blend, providing fundamental research on the Ti₃Al lattice structure by LPBF. With the starting feedstock of CP-Ti and TiAl-4822 powder blends, the as-built strut sample showed good chemical homogeneity in the central region with some partially-melted particles in the peripheral regions. With the aid of the high cooling rate, a high volume fraction of the β phase was achieved to lower the cracking susceptibility. After the heat treatment of 1200 °C for 4 h, the partially-melted Ti particles were fully dissolved, and an α_2/β dual-phase structure was achieved. The equiaxed α_2 grains contained a volume fraction of 60.3%, with a grain size of $15 \pm 4.7 \mu\text{m}$. The precipitation of α_2 grains from β grains followed the Burgers orientation relationship. The microhardness was measured to be $515 \pm 38 \text{ HV}$ in the as-built sample. After the heat treatment of 1200 °C for 4 h, the microhardness changed to $475 \pm 37 \text{ HV}$. This study demonstrated a method to fabricate crack-free intermetallic components, which was considered inapplicable to LPBF, using a powder blend. Future studies in this field can be the lattice structure components fabrication, the scaling up of the thin strut, and the investigation of the effect of heat treatment, etc.

Author Contributions: Conceptualization, K.L., X.W.; methodology, K.L., X.W., H.C. and X.H.; validation, K.L., X.W. and G.Z.; formal analysis, K.L., X.W., X.H., and G.Z.; investigation, K. L. and X.W.; resources, K.L., X.H. and H.C.; writing—original draft preparation, K.L.; writing—review and editing, K.L., X.W., X.H., G.Z. and G.T.; visualization, K.L. and X.W.; supervision, G.T.; project administration, X.H, H.C.; funding acquisition, K.L., X.H. and H.C. All authors have read and agreed to the published version of the manuscript.

Funding: This research was funded by Wenzhou Science and Technology Association Service Technology Innovation Project, grant number kjfw12, Scientific Research Fund of Zhejiang Provincial Education Department Project No. Y202146845, and Wenzhou Public Welfare Science and Technology Plan Project No. G20210018.

Data Availability Statement: Data will be made available on reasonable request.

Conflicts of Interest: The authors declare no conflict of interest.

References

1. Djanarthany, S.; Viala, J.-C.; Bouix, J. An overview of monolithic titanium aluminides based on Ti₃Al and TiAl. *Mater. Chem. Phys.* **2001**, *72*, 301–319. [[CrossRef](#)]
2. Clemens, H.; Mayer, S. Intermetallic titanium aluminides in aerospace applications—processing, microstructure and properties. *Mater. High Temp.* **2016**, *33*, 560–570. [[CrossRef](#)]
3. Froes, F.; Suryanarayana, C. Titanium aluminides. *Phys. Metall. Process. Intermet. Compd.* **1996**, 297–350. [[CrossRef](#)]
4. Hegab, H.A. Design for additive manufacturing of composite materials and potential alloys: A review. *Manuf. Rev.* **2016**, *3*, 11. [[CrossRef](#)]
5. Bandyopadhyay, A.; Traxel, K.D.; Lang, M.; Juhasz, M.; Eliaz, N.; Bose, S. Alloy design via additive manufacturing: Advantages, challenges, applications and perspectives. *Mater. Today* **2022**, *52*, 207–224. [[CrossRef](#)]
6. Murr, L.E.; Martinez, E.; Amato, K.N.; Gaytan, S.M.; Hernandez, J.; Ramirez, D.A.; Shindo, P.W.; Medina, F.; Wicker, R.B. Fabrication of metal and alloy components by additive manufacturing: Examples of 3D materials science. *J. Mater. Res. Technol.* **2012**, *1*, 42–54. [[CrossRef](#)]
7. Murr, L.E.; Gaytan, S.M.; Ceylan, A.; Martinez, E.; Martinez, J.L.; Hernandez, D.H.; Machado, B.I.; Ramirez, D.A.; Medina, F.; Collins, S. Characterization of titanium aluminide alloy components fabricated by additive manufacturing using electron beam melting. *Acta Mater.* **2010**, *58*, 1887–1894. [[CrossRef](#)]
8. Yue, H.; Chen, Y.; Wang, X.; Kong, F. Effect of beam current on microstructure, phase, grain characteristic and mechanical properties of Ti-47Al-2Cr-2Nb alloy fabricated by selective electron beam melting. *J. Alloys Compd.* **2018**, *750*, 617–625. [[CrossRef](#)]
9. Todai, M.; Nakano, T.; Liu, T.; Yasuda, H.Y.; Hagihara, K.; Cho, K.; Ueda, M.; Takeyama, M. Effect of building direction on the microstructure and tensile properties of Ti-48Al-2Cr-2Nb alloy additively manufactured by electron beam melting. *Addit. Manuf.* **2017**, *13*, 61–70. [[CrossRef](#)]
10. Ma, Y.; Cuiuri, D.; Li, H.; Pan, Z.; Shen, C. The effect of postproduction heat treatment on γ -TiAl alloys produced by the GTAW-based additive manufacturing process. *Mater. Sci. Eng. A* **2016**, *657*, 86–95. [[CrossRef](#)]

11. Sharman, A.R.C.; Hughes, J.I.; Ridgway, K. Characterisation of titanium aluminide components manufactured by laser metal deposition. *Intermetallics* **2018**, *93*, 89–92. [[CrossRef](#)]
12. Wang, H.; Fang, Z.Z.; Sun, P. A critical review of mechanical properties of powder metallurgy titanium. *Int. J. Powder Metall.* **2010**, *46*, 45–57.
13. Chen, Y.; Zhang, X.; Parvez, M.M.; Liou, F. A Review on Metallic Alloys Fabrication Using Elemental Powder Blends by Laser Powder Directed Energy Deposition Process. *Materials* **2020**, *13*, 3562. [[CrossRef](#)] [[PubMed](#)]
14. Wang, C.; Tan, X.; Du, Z.; Chandra, S.; Sun, Z.; Lim, C.; Tor, S.; Lim, C.; Wong, C. Additive manufacturing of NiTi shape memory alloys using pre-mixed powders. *J. Mater. Process. Technol.* **2019**, *271*, 152–161. [[CrossRef](#)]
15. Yan, L.; Chen, X.; Li, W.; Newkirk, J.; Liou, F. Direct laser deposition of Ti-6Al-4V from elemental powder blends. *Rapid Prototyp. J.* **2016**, *22*, 810–816. [[CrossRef](#)]
16. Chen, X. *Fabrication and Characterization of Advanced Materials Using Laser Metal Deposition from Elemental Powder Mixture*; Missouri University of Science and Technology: Rolla, MO, USA, 2018.
17. Li, W.; Yan, L.; Chen, X.; Zhang, J.; Zhang, X.; Liou, F. Directed energy depositing a new Fe-Cr-Ni alloy with gradually changing composition with elemental powder mixes and particle size effect in fabrication process. *J. Mater. Process. Technol.* **2018**, *255*, 96–104. [[CrossRef](#)]
18. Grigoriev, A.; Polozov, I.; Sufiiarov, V.; Popovich, A. In-situ synthesis of Ti₂AlNb-based intermetallic alloy by selective laser melting. *J. Alloys Compd.* **2017**, *704*, 434–442. [[CrossRef](#)]
19. Polozov, I.; Sufiiarov, V.; Kantuykov, A.; Popovich, A. Selective Laser Melting of Ti₂AlNb-based intermetallic alloy using elemental powders: Effect of process parameters and post-treatment on microstructure, composition, and properties. *Intermetallics* **2019**, *112*, 106554. [[CrossRef](#)]
20. Jicai, F.; Huiqiang, W.; Jingshan, H.; Bingang, Z. Microstructure evolution of electron beam welded Ti₃Al–Nb joint. *Mater. Charact.* **2005**, *54*, 99–105. [[CrossRef](#)]
21. Balla, V.K.; Das, M.; Mohammad, A.; Al-Ahmari, A.M. Additive Manufacturing of γ -TiAl: Processing, Microstructure, and Properties. *Adv. Eng. Mater.* **2016**, *18*, 1208–1215. [[CrossRef](#)]
22. Dzogbewu, T.C.; du Preez, W.B. Additive manufacturing of Ti-based intermetallic alloys: A review and conceptualization of a next-generation machine. *Materials* **2021**, *14*, 4317. [[CrossRef](#)] [[PubMed](#)]
23. DebRoy, T.; Wei, H.L.; Zuback, J.S.; Mukherjee, T.; Elmer, J.W.; Milewski, J.O.; Beese, A.M.; Wilson-Heid, A.; De, A.; Zhang, W. Additive manufacturing of metallic components—Process, structure and properties. *Prog. Mater. Sci.* **2018**, *92*, 112–224. [[CrossRef](#)]
24. Yakovenkova, L.; Malinov, S.; Karkina, L.; Novoselova, T. Crack geometry for basal slip of Ti₃Al. *Scr. Mater.* **2005**, *52*, 1033–1038. [[CrossRef](#)]
25. Her, Y.; Yang, J.-M.; Wang, P. Effect of fiber coating on the fatigue crack initiation and multiplication of unnotched SCS-6/Ti₃Al composites. *Mater. Sci. Eng. A* **1999**, *259*, 201–208. [[CrossRef](#)]
26. Chen, W.; Li, Z. Additive manufacturing of titanium aluminides. In *Additive Manufacturing for the Aerospace Industry*; Elsevier: Beijing, China, 2019; pp. 235–263.
27. Zhang, Y.; Wang, X.; Kong, F.; Sun, L.; Chen, Y. A high-performance β -solidifying TiAl alloy sheet: Multi-type lamellar microstructure and phase transformation. *Mater. Charact.* **2018**, *138*, 136–144. [[CrossRef](#)]
28. Cho, W.; Thompson, A.W.; Williams, J.C. Creep behavior of Ti-25Al-10Nb-3V-1Mo. *Metall. Trans. A* **1990**, *21*, 641–651. [[CrossRef](#)]
29. Vaidya, R.U.; Park, Y.S.; Zhe, J.; Gray, G.T.; Butt, D.P. High-temperature oxidation of Ti-48Al-2Nb-2Cr and Ti-25Al-10Nb-3V-1Mo. *Oxid. Met.* **1998**, *50*, 215–240. [[CrossRef](#)]
30. Suwas, S.; Ray, R. Evolution of texture in the β (B2) phase of a two phase titanium aluminide intermetallic alloy Ti-24Al-11Nb. *Metall. Mater. Trans. A* **2000**, *31*, 2339–2350. [[CrossRef](#)]
31. Li, S.; Lau, K.B.; Wu, D.; Wei, F.; Lin, M.; Cheong, A.; Wang, P.; Tan, C.C.; Ramamurty, U. 3D printing of ductile equiatomic Fe-Co alloy for soft magnetic applications. *Addit. Manuf.* **2021**, *47*, 102291. [[CrossRef](#)]
32. Durejko, T.; Ziętala, M.; Łazińska, M.; Lipiński, S.; Polkowski, W.; Czujko, T.; Varin, R.A. Structure and properties of the Fe₃Al-type intermetallic alloy fabricated by laser engineered net shaping (LENS). *Mater. Sci. Eng. A* **2016**, *650*, 374–381. [[CrossRef](#)]
33. Li, K.; Wang, X.; Brodusch, N.; Tu, G. Mitigating cracking in laser powder bed fusion of Ti-48Al-2Cr-2Nb via introducing massive β phase. *Mater. Charact.* **2023**, *196*, 112558. [[CrossRef](#)]
34. Holec, D.; Legut, D.; Isaeva, L.; Souvatzis, P.; Clemens, H.; Mayer, S. Interplay between effect of Mo and chemical disorder on the stability of β / β -TiAl phase. *Intermetallics* **2015**, *61*, 85–90. [[CrossRef](#)]
35. Clemens, H.; Wallgram, W.; Kremmer, S.; Güther, V.; Otto, A.; Bartels, A. Design of Novel β -Solidifying TiAl Alloys with Adjustable β /B2-Phase Fraction and Excellent Hot-Workability. *Adv. Eng. Mater.* **2008**, *10*, 707–713. [[CrossRef](#)]
36. Kaufman, M.J. *Phase Relations in the Ti₃Al+ Nb System*; Washington Univ Seattle Dept of Materials Science and Engineering: Seattle, WA, USA, 1988.
37. Elmer, J.; Allen, S.; Eagar, T. Microstructural development during solidification of stainless steel alloys. *Metall. Trans. A* **1989**, *20*, 2117–2131. [[CrossRef](#)]
38. Sung, S.-Y.; Kim, Y.-J. Modeling of titanium aluminides turbo-charger casting. *Intermetallics* **2007**, *15*, 468–474. [[CrossRef](#)]
39. Aziz, M.J.; Kaplan, T. Continuous growth model for interface motion during alloy solidification. *Acta Metall.* **1988**, *36*, 2335–2347. [[CrossRef](#)]

40. Gogia, A.; Banerjee, D.; Nandy, T. Structure, tensile deformation, and fracture of a Ti-3Al-Nb alloy. *Metall. Trans. A* **1990**, *21*, 609–625. [[CrossRef](#)]
41. Wu, Y.; Yang, C.; Koo, C.; Singh, A. A study of texture and temperature dependence of mechanical properties in hot rolled Ti-25Al-xNb alloys. *Mater. Chem. Phys.* **2003**, *80*, 339–347. [[CrossRef](#)]
42. Kumar, S.; Reddy, R. Microstructure and phase relations in a powder-processed Ti-22Al-12Nb Alloy. *Metall. Mater. Trans. A* **1996**, *27*, 1121–1126. [[CrossRef](#)]
43. Strychor, R.; Williams, J.; Soffa, W. Phase transformations and modulated microstructures in Ti-Al-Nb alloys. *Metall. Trans. A* **1988**, *19*, 225–234. [[CrossRef](#)]
44. Sircar, S.; Narasimhan, K.; Mukherjee, K. An investigation of the ordered DO 19 phase formation in the Ti-Al system. *J. Mater. Sci.* **1986**, *21*, 4143–4146. [[CrossRef](#)]
45. Ding, H.; Song, D.; Wang, D.; Zhang, C.; Cui, J. Microstructural evolution in superplastic deformation of a Ti3Al alloy. *J. Mater. Sci. Lett.* **2000**, *13*, 1135–1137. [[CrossRef](#)]
46. Wang, X.; Muñoz-Lerma, J.A.; Sánchez-Mata, O.; Attarian Shandiz, M.; Brochu, M. Microstructure and mechanical properties of stainless steel 316L vertical struts manufactured by laser powder bed fusion process. *Mater. Sci. Eng. A* **2018**, *736*, 27–40. [[CrossRef](#)]
47. Yu, C.-H.; Peng, R.L.; Luzin, V.; Sprengel, M.; Calmunger, M.; Lundgren, J.-E.; Brodin, H.; Kromm, A.; Moverare, J. Thin-wall effects and anisotropic deformation mechanisms of an additively manufactured Ni-based superalloy. *Addit. Manuf.* **2020**, *36*, 101672. [[CrossRef](#)]
48. Schuster, J.C.; Palm, M. Reassessment of the binary Aluminum-Titanium phase diagram. *J. Phase Equilibria Diffus.* **2006**, *27*, 255–277. [[CrossRef](#)]
49. Tong, V.; Joseph, S.; Ackerman, A.K.; Dye, D.; Britton, T.B. Using transmission Kikuchi diffraction to characterise α variants in an $\alpha + \beta$ titanium alloy. *J. Microsc.* **2017**, *267*, 318–329. [[CrossRef](#)] [[PubMed](#)]
50. Gao, X.; Zeng, W.; Li, X.; Zhou, D.; Xu, J.; Wang, Q. Effect of boundary on the alpha phase precipitation in a near-alpha titanium alloy. *Mater. Lett.* **2018**, *233*, 298–301. [[CrossRef](#)]
51. Chen, F.-W.; Xu, G.; Zhang, X.-Y.; Zhou, K.-C.; Cui, Y. Effect of α morphology on the diffusional $\beta \leftrightarrow \alpha$ transformation in Ti-55531 during continuous heating: Dissection by dilatometer test, microstructure observation and calculation. *J. Alloys Compd.* **2017**, *702*, 352–365. [[CrossRef](#)]
52. Pang, G.-D.; Lin, Y.; Jiang, Y.-Q.; Zhang, X.-Y.; Liu, X.-G.; Xiao, Y.-W.; Zhou, K.-C. Precipitation behaviors and orientation evolution mechanisms of α phases in Ti-55511 titanium alloy during heat treatment and subsequent hot deformation. *Mater. Charact.* **2020**, *167*, 110471. [[CrossRef](#)]
53. Bhattacharyya, D.; Viswanathan, G.; Denkenberger, R.; Furrer, D.; Fraser, H.L. The role of crystallographic and geometrical relationships between α and β phases in an α/β titanium alloy. *Acta Mater.* **2003**, *51*, 4679–4691. [[CrossRef](#)]
54. Wu, X.; Cai, C.; Yang, L.; Liu, W.; Li, W.; Li, M.; Liu, J.; Zhou, K.; Shi, Y. Enhanced mechanical properties of Ti-6Al-2Zr-1Mo-1V with ultrafine crystallites and nano-scale twins fabricated by selective laser melting. *Mater. Sci. Eng. A* **2018**, *738*, 10–14. [[CrossRef](#)]
55. Liu, J.; Li, Y.; Zhu, Y.; Yang, Y.; Zhang, R.; Zhang, Z.; Huang, A.; Zhang, K. Enhancing high-temperature strength and ductility in laser powder bed fusion Ti-6.5Al-2Zr-1Mo-1V alloy via heat treatment optimization. *Mater. Sci. Eng. A* **2022**, *859*, 144201. [[CrossRef](#)]
56. Brandl, E.; Greitemeier, D. Microstructure of additive layer manufactured Ti-6Al-4V after exceptional post heat treatments. *Mater. Lett.* **2012**, *81*, 84–87. [[CrossRef](#)]
57. Li, X.; He, J.; Zhang, T.; Tao, J.; Li, J.; Zhang, Y. Effect of heat treatment on the microstructure and properties of a Ti3Al linear friction welding joint. *Materials* **2019**, *12*, 1159. [[CrossRef](#)]
58. Chen, W.; Chen, Z.Y.; Wu, C.C.; Li, J.W.; Tang, Z.Y.; Wang, Q.J. The effect of annealing on microstructure and tensile properties of Ti-22Al-25Nb electron beam weld joint. *Intermetallics* **2016**, *75*, 8–14. [[CrossRef](#)]

Disclaimer/Publisher’s Note: The statements, opinions and data contained in all publications are solely those of the individual author(s) and contributor(s) and not of MDPI and/or the editor(s). MDPI and/or the editor(s) disclaim responsibility for any injury to people or property resulting from any ideas, methods, instructions or products referred to in the content.